Transport phenomena at test and control lines in lateral flow immunoassays reveal a path to expanding their dynamic range

Sathishkumar N[1], Bhushan J. Toley[1*]

[1]Department of Chemical Engineering
Indian Institute of Science
Bengaluru, Karnataka 560012
India

* Correspondence to:
Bhushan J. Toley
Department of Chemical Engineering
Indian Institute of Science
C V Raman Avenue
Bengaluru, Karnataka 560012
Phone: +91-80-2293-3114
E-mail: bhushan@iisc.ac.in

ORCIDs
Bhushan Toley: 0000-0003-0119-2350
Sathishkumar N: 0000-0003-1174-2256

Keywords: Lateral flow assay, dynamic range, hook effect, transport-reaction modelling

Abstract

This study presents theoretical underpinnings for how the dynamic range of a lateral flow immunoassay (LFIA) may be expanded by real-time imaging. The dynamic range of a sandwich LFIA is limited by the 'hook effect', according to which, test line signal intensities reduce with increasing analyte concentration beyond a threshold analyte concentration. Rey et al. (*Anal Chem*, 2017, 89(9)) have shown experimentally that the hook effect in sandwich LFIAs may be mitigated by real-time imaging of test and control line, but theoretical understanding of the transport phenomena that govern this phenomenon is lacking. In fact, transport phenomena at the control line of an LFIA have never been modelled. In this paper, we use a transport-reaction model to understand how the kinetics of signal generation at the test and control lines of an LFIA relate to analyte concentration. Using this model, we developed a method for determination of analyte concentration accurately over a much larger range than the traditional end-point detection method. The model was validated using a commercially available lateral flow assay (home pregnancy test) on which real time imaging was conducted using a time-lapse app on a smartphone; there was a strong agreement between the predictions of our model and experiments results. The newly developed readout method increased the dynamic range for the detection of human chorionic gonadotropin (hCG) to 3 orders of magnitude (compared to ~1.5 orders of magnitude achieved by traditional end-point detection), without any modification to the test strip.

Introduction

The lateral flow immunoassay (LFIA) is the one of most successful rapid diagnostic test (RDT) for point-of-care testing. Although improving sensitivity and quantification remain the major areas of focus of the LFIA research community, widening the dynamic range to capture the entire clinically relevant range of an analyte is equally important. The concentrations of diagnostically important analytes such as carcinoembryonic antigen (CEA), calcitonin, prolactin and C-reactive protein (CRP) can vary over a wide range and have different clinical implications depending on their concentration range (1–4).

The dynamic range of LFIAs based on the sandwich format roughly spans 1.5 orders of magnitude (5–7) and is limited by the 'hook effect', according to which test line signal intensities reduce with increasing analyte concentration beyond a threshold analyte concentration (8, 9). The reduction in test line intensity is a result of the need for a bivalent interaction between a single antigen molecule and two antibody molecules (capture and detection antibodies) for the signal to develop. Above a threshold antigen concentration, the probability of such a bivalent interaction decreases because the available capture and detection antibodies are more likely to bind with different antigen molecules. The 'hook effect' may lead to either false negative results or underestimation of the concentration of the analyte being detected. The threshold analyte concentration at which the 'hook effect' sets in can be changed by adjusting antibody concentrations (10, 11), but this simply shifts the dynamic range of the LFIA as opposed to expanding it. Attempts been made to mitigate the 'hook effect' and expand the dynamic range of LFIAs include serial dilution of test samples(12), increasing the number of test lines(13), addition of unlabelled capture and detection antibodies to the sample at higher analyte concentrations(14), and sequentially delivering the antigen and conjugated detection antibody to the test zone by incorporating certain design changes into the LFIA(3). Recently,

Gasperino et al., showed that the graded ladder bar format could be a useful tool for applications requiring quantification of sample concentrations over a wide range(7). Except serial sample dilution (which increases the number of user steps), none of the above methods can be used with off-the-shelf commercially available LFIAs.

A method for expanding the dynamic range of LFIAs employing time-lapse imaging of the test and control lines was recently demonstrated by Rey et al.(15). They showed that the real-time progression of the ratios of test line to control line intensities (*T/C* ratio) reported the analyte concentration over a wider range compared to end point intensity of the test line. To demonstrate this, they built an in-house LFIA for detection of C-reactive protein (CRP). Although an elegant demonstration, the fundamental transport-reaction phenomena that govern the real time progression of the *T/C* ratio and how this time progression relates to antigen concentration is not understood. In fact, although several transport-reaction models of LFIAs have been developed (11, 16–19), all these models only concern the development of signal at the test line; transport phenomena at the control line of an LFIA have not been studied.

In this work, we provide fundamental understanding of how the antigen concentration in an LFIA affects the dynamics of signal development at the test and control lines and thereby the *T/C* ratio. Using this understanding, we developed a method to expand the dynamic range of a commercially available home pregnancy test to up to three orders of magnitude without making any modifications to the test device. The developed strategy requires only a cell phone camera, a time-lapse imaging app, and a small custom-made imaging box. This new method will enable developing LFIAs having a wider dynamic range for analyte quantitation without compromising the limit of detection. Given that smartphones are ubiquitous, this method has

the potential to significantly enhance the utility of an already successful and prevalent point-of-care diagnostic modality.

Experimental Section

Three commercially available pregnancy kits: 1) 'Am I', Microsidd, India, 2) 'Prega', Mankind Pharma Ltd, Paonta Sahib, HP, India, and 3) 'i-Can', Piramal, Mumbai, India, were subjected to spiked human chorionic gonadotropin (hCG) samples (Sigma Aldrich, US) in distilled water. Time-lapse images of test and control lines at intervals of 1s were obtained in a custom-made imaging box using a cell phone (Redmi 5) equipped with Framelapse App (Neximo Labs, UP, India). All image analyses were conducted in ImageJ. Colored images were split into three color channels and the green channel was chosen for analysis. Rectangular regions of interest (ROIs) were created around the test and control lines and ROIs of equal size were created immediately upstream and immediately downstream of the test and control lines for measurement and subtraction of background signals, as illustrated in Supplementary Information Section S1.

Results

Experimental measurement of the kinetics of signal generation in LFIA's

DI water containing increasing concentrations of human chorionic gonadotropin (hCG) was introduced into commercial home pregnancy tests (Am I pregnancy kit, Microsidd, Bangalore, India). The end-point (10 min) test line intensity, I_{end}, increased with increasing hCG concentration in the range of 0.5 – 40 international units/ml (IU/ml) and reduced with increasing hCG concentrations in the range of 40 – 500 IU/ml, demonstrating 'the hook effect' (Fig. 1A,B). A similar trend was observed with the end-point (10 min) test line to control line intensity ratio, T/C_{end} (Fig. 1C). Quantification of analytes using LFIAs based only on either

I_{end} or T/C_{end} could therefore be erroneous. For example, I_{end} was approximately equal for hCG concentrations of 10 and 80 IU/mL (Fig. 1B). However, although I_{end} for these two concentrations was equal, the kinetics of signal generation at the test and control lines for these two cases was different. For example, the test line for 10 IU/ml developed slower than for 80 IU/ml (Fig. 1D, F). A more quantitative measure is the rate of change of T/C ratios for the two cases. As an illustration, at t = 100s, d/dt (T/C) was positive for 10 IU/mL (Fig. 1E) and negative for 80 IU/mL (Fig. 1G). d/dt (T/C) was calculated by subtracting T/C value at t=100s from t=101s and dividing it by Δt=1s Measurement of the kinetics of signal generation at the test and control lines thereby presents an opportunity to alleviate the hook effect.

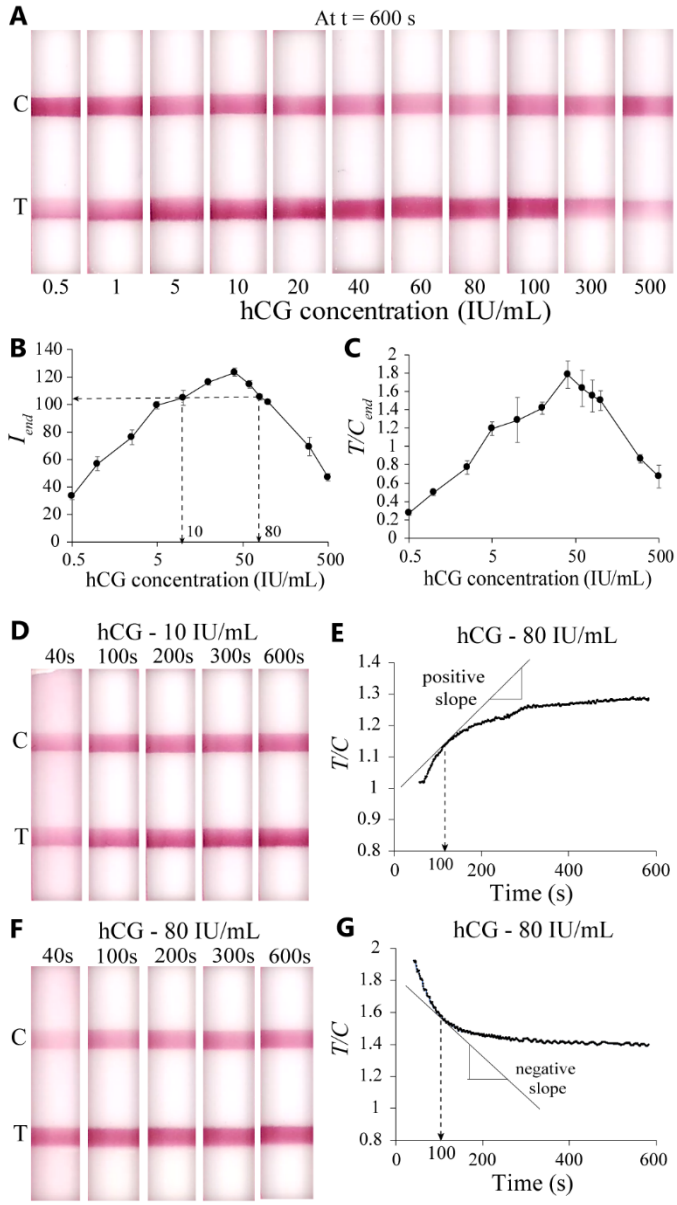

Figure 1: Experimental measurement of signal generation in lateral flow immunoassays. A. End-point (t=600s) images of hCG LFIAs for different hCG concentrations. **B.** Plot of I_{end} vs hCG concentration shows that I_{end} increased from 0 – 40 and reduced from 40 – 500 IU/ml hCG. I_{end} for 10 and 80 IU/mL were approximately equal. **C.** Plot of T/C_{end} vs hCG concentration shows that T/C_{end} increased from 0 – 40 and reduced from 40 – 500 IU/ml hCG. For B and C, error bars represent standard deviations (N=3). **D-G.** Kinetics of signal generation at test and control lines showing time-lapse images for 10 IU/ml (**D**) and 80 IU/ml (**F**) and plots of T/C ratio vs time for 10 IU/ml (**E**) and 80 IU/ml (**G**). At 100s, the plot for T/C vs time had a positive slope for 10 IU/ml (D) and negative slope for 80 IU/ml (F).

Modelling transport phenomena at the test and control lines of an LFIA

In order to develop a thorough understanding of the kinetics of signal generation at the test and control lines, a mathematical model of transport and reaction phenomena in these zones was

developed. The modelling domain is shown in Figure 2A. The length of the domain was 2 cm and the lengths of test and control zones (lines) were 1 mm. The capture antibody (R) and the control line antibody (Q) were assumed to be immobilized in the test and control zones respectively. A sample consisting of a dilute analyte (A) premixed with a detection antibody-gold nanoparticle conjugate (reporter particle; P) was flowed into the domain with a velocity, v. In experiments, the reporter particles were dry stored in 'conjugate pads' by the manufacturer of the lateral flow assay, but for the model they were assumed to be premixed with the analyte. The following reactions occur in the domain (refer to Figure 2A). Analyte (A) from the sample binds with reporter particle (P) to form analyte-reporter complex (PA), A + P ⇄ PA. The mixture of A, P and PA migrates to the capture zones. The capture antibody (R) at the test line captures the analyte (A), R + A ⇄ RA and the analyte-reporter complex (PA), R + PA ⇄ RPA. Unbound reporter particle (P) interact with RA forming RA + P ⇄ RPA. The species RPA was the signal forming complex at the test line. At the control line, P and PA get captured by control line antibody (Q); Q + P ⇄ QP and Q + PA ⇄ QPA. QP may further interact with free A; QP + A ⇄ QPA. Both QP and QPA were the signal forming complexes at the control line. The species transport-reaction equation for all the species was as follows:

$$\frac{\partial C_i}{\partial t} = D_i \frac{\partial C_i^2}{\partial x^2} - v.\left(\frac{\partial C_i}{\partial x}\right) - r_i \quad \text{----- Eq 1}$$

where C_i is the concentration, D_i is the diffusion coefficient, v is the fluid flow velocity, and r_i is the reaction rate (formation or consumption) of the i^{th} species. The complete list of equations for each species is provided in Supplementary Information Section S2. The set of coupled partial differential equations was discretized over space using finite central differences (Supplementary Information Section S3). This generated a set of ordinary differential equations, which was solved using the inbuilt ode23s solver in MATLAB to obtain the concentrations of all species over space and time. The flow velocity, v, was set to 0.3333 mm/s to match the average velocity measured under these conditions in other lateral flow strips made

from nitrocellulose NCFF120 (GE Whatman) in our lab. The values of diffusivities and reaction rate constants were obtained from Qian and Lin et al (16, 20).

Consistent with what was observed experimentally, the plot of I_{end}, i.e. the concentrations of signal forming species RPA at the test line, against analyte concentration displayed the hook effect beyond an analyte concentration of $5x10^{-8}$ M (Fig. 2B). The model further showed that the *T/C* ratio had different time profiles for low, high and very high analyte concentrations (Fig. 2C). For low analyte concentrations ($5x10^{-10}$ to $5x10^{-9}$ M), the *T/C* ratio increased monotonously; for high analyte concentrations ($1x10^{-8}$ to $1x10^{-7}$ M), the *T/C* ratio initially increased and then decreased; for very high analyte concentrations ($5x10^{-7}$ to $5x10^{-6}$ M), the *T/C* ratio decreased monotonously (Fig. 2C). Intuitively, this can be understood as follows. At low analyte concentration, the kinetics of analyte binding and signal generation at the test line is slow while the control line signal develops and saturates rapidly as a large concentration of unreacted reporter particles flow over it. The intensity of the test line increases slowly but the control line is already saturated. Therefore, the *T/C* ratio increases monotonously. Conversely, at high analyte concentration, the test line develops rapidly but the control line develops slowly, causing the T/C ratio to decrease monotonously. Therefore, according to this model, if I_{end} alone were used as a parameter to back calculate analyte concentration, the dynamic range would be limited to $5x10^{-10}$ to $5x10^{-8}$ M, bounded at the upper end by the onset of the hook effect. However, the time profiles of *T/C* ratio vary considerably over the entire range of analyte concentrations ranging from $5x10^{-10}$ to $1x10^{-6}$ M and could be used to distinguish between analyte concentrations in the entire range. Note that at a concentration of $1x10^{-6}$ M, the *T/C* ratio is close to zero for the entire time period (Fig. 2C), representing the theoretical upper limit for quantification using the LFIA. Experimental profiles of *T/C* ratio qualitatively matched the

model's predictions and displayed the three distinct types of *T/C* ratio time profiles with increasing analyte concentration (Supplementary Information Section S4).

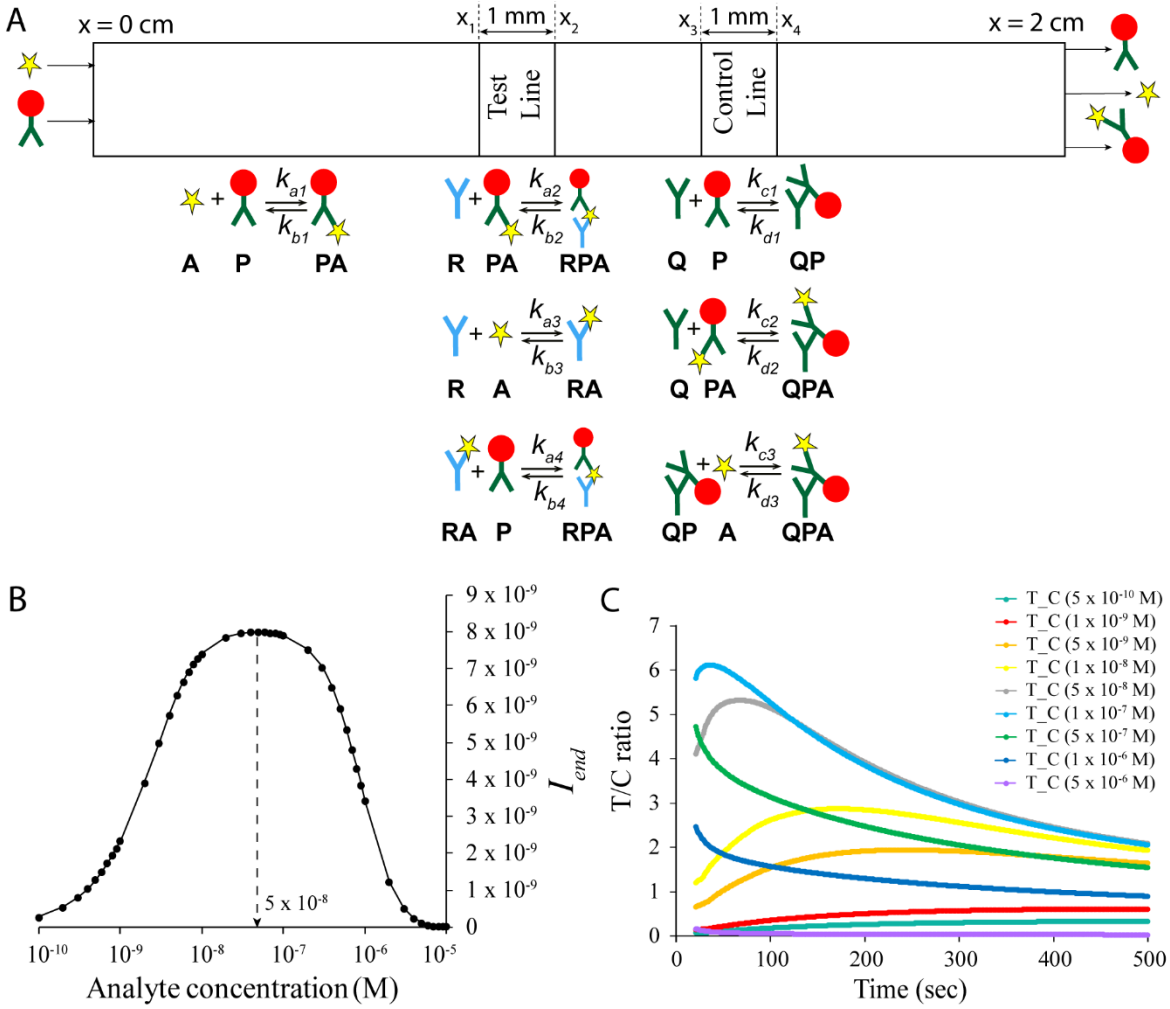

Figure 2: Transport reaction modelling of the test and control zones. A. The modelling domain. The length of the strip was 2 cm and the width of both test and control lines was 1 mm. **B.** The hook effect in I_{end} observed after an analyte concentration of 5×10^{-8} M. **C**. Plots of *T/C* ratio vs time showing different types of profiles with varying analyte concentrations.

Empirical fitting of *T/C* ratio time profiles

Because the profiles of *T*/*C* vs time respond to changing analyte concentrations over a wide concentration range, it was desirable to represent each time profile by a set of parameters. When plotted against the analyte concentration, these parameters would constitute a new calibration

curve having a significantly wider dynamic range. With this objective, the profiles were fit to a biexponential expression:

$$T/C = a.e^{bt} + c.e^{dt} \text{ ------ Eq 2}$$

using the nonlinear least squares method in MATLAB curve fitting toolbox. First, T/C time profiles obtained from the mathematical model were fit and the variation of parameters '*a*', '*b*', '*c*', and '*d*' with respect to analyte concentration was analysed. The pre-exponents '*a*' and '*c*' varied monotonously with analyte concentration (with '*c*' mirroring '*a*' across the x-axis) till the onset of hook effect (Fig 3A). For analyte concentrations beyond the onset of hook effect (> $5x10^{-8}$M), '*c*' did not show a consistent trend, while '*a*' monotonously decreased with increasing analyte concentration. The parameter '*a*' thus exhibited a hook effect-like trend, similar to I_{end} and therefore does not enable expanding the dynamic range. Next, the exponents '*b*' and '*d*' were analysed. The exponent '*b*' did not vary with increasing analyte concentration till the onset of hook effect but decreased monotonously for analyte concentrations beyond the onset of the hook effect (Fig 3B). Whereas the exponent '*d*' decreased monotonously with increasing analyte concentration till the onset of hook effect and was fairly irresponsive to changes in analyte concentration beyond that (Fig. 3B).

Based on the above observation, we hypothesized that a combination of I_{end} and '*b*' would enable determination of analyte concentration well beyond the onset of hook effect and proposed the following strategy. Let the range of analyte concentrations below the onset of hook effect be referred to as Zone I and above as Zone II (Fig. 3C). Note that $b > -0.0025$ for Zone I and $b < -0.0025$ for Zone II (Fig. 3C). Therefore, evaluation of parameter '*b*' determines which zone the analyte concentration lies in. Now, in Zone I, the parameter 'I_{end}' may be used for quantification as it increases monotonously with analyte concentration, whereas in Zone II, the parameter '*b*' may be used as it decreases monotonously.

In order to validate the proposed method of analyte quantification, experiments were conducted by introducing varying concentrations of hCG solutions into commercially available pregnancy test strips, time-lapse images were acquired, images were analysed to estimate *T/C* ratio as a function of time, and the profiles were fit to the biexponential form in Equation 2 to determine parameters '*a*', '*b*', '*c*', and '*d*'. Figure 3D shows the variation of parameter '*a*' and '*c*'; Figure 3E shows the variation of parameter '*b*' and '*d*'. The response of all parameters was qualitatively equivalent to that obtained from the model (Fig. 3A-B) and thus validates our model. Most importantly, the parameter '*b*' exhibited the desired behavior, i.e. i) $b > -0.0025$ for Zone I and $b < -0.0025$ for Zone II, and ii) '*b*' decreased monotonously with increasing analyte concentration in Zone II (Fig. 3E). When experimentally obtained I_{end} and '*b*' were plotted over the entire range of analyte concentrations, their response was in strong agreement with the model predictions (Fig. 3F). This plot of I_{end} and '*b*' (Fig. 3F) is the new calibration curve for this LFIA with a proposed dynamic range of three orders of magnitude (0.5 – 500 IU/ml; Fig. 3F).

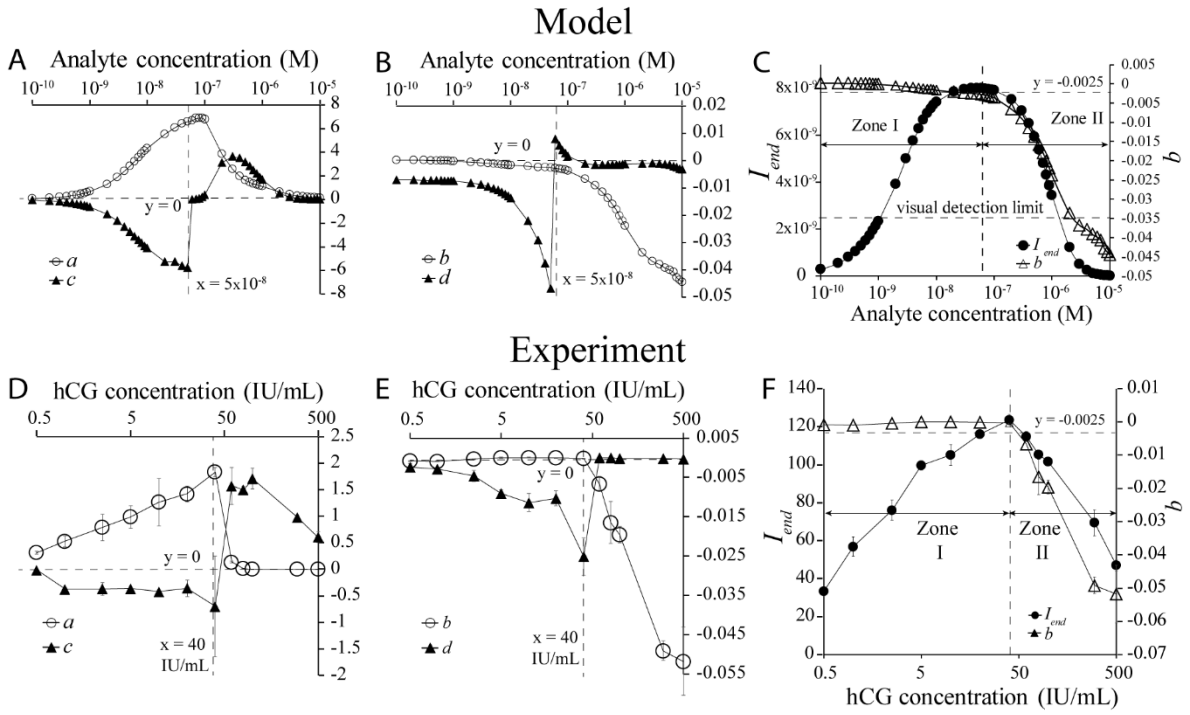

Figure 3. Parameters obtained from fitting modelled and experimental data. **A-C.** Plots of parameters '*a*' and '*c*' (**A**); '*b*' and '*d*' (**B**), and I_{end} and '*b*' (**C**) as a function of analyte concentration obtained from fitting mathematically modelled profiles of *T/C* ratio vs time. **D-F**. Corresponding plots obtained from fitting experimentally measured profiles of *T/C* ratio vs time. For all experiments, error bars represent standard deviations (N=3).

Demonstration of the expansion of dynamic range of an LFIA using the proposed method

A set of solutions with known hCG concentrations ranging from 0.5 to 500 IU/ml were prepared and introduced into commercially available home pregnancy test strips, followed by time-lapse imaging of the test and control lines. The concentration of hCG was measured from the strip using two methods – i) the traditional end-point detection method based on I_{end} alone, and ii) our proposed method using time-lapse imaging and measurement of I_{end} and parameter '*b*'. Relationship between actual (x-axis) and measured (y-axis) hCG concentrations obtained using the two methods are shown in Figures 4A (end-point method) and 4B (time-lapse method). The 45° line shows the ideal linear relationship between measured and actual concentrations. Mean and standard deviations for three separate measurements are shown. While using the conventional method of measuring only I_{end}, the measured hCG concentrations were accurate at low concentrations but showed large deviations at concentrations beyond 50

IU/ml because of the onset of hook effect (Fig. 4A). The calibration curve used to make these measurements is the plot of I_{end} vs hCG concentration in Zone I of Fig. 3F. Thus, the quantification of analytes using LFIAs based only on I_{end} leads to poor predictions. While using the time-lapse-based method for measurement, i.e. using the combined calibration curves in Zones I and II of Fig. 3F, the measured hCG concentrations were accurate over the entire range (Fig. 4B). This is a significant expansion over the dynamic range afforded by the traditional end-point method.

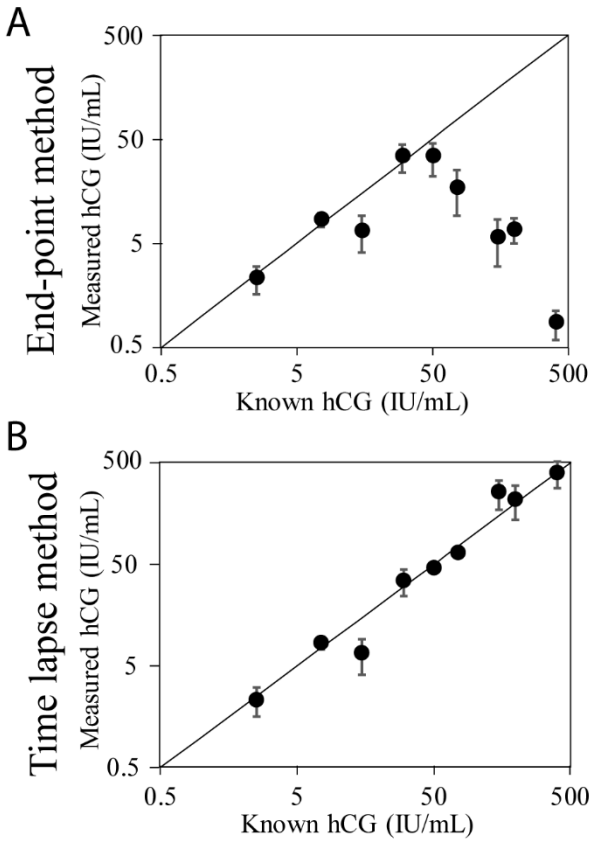

Figure 4. Measurement of analyte concentrations using end-point and time-lapse methods. A. Measured vs known hCG concentrations using the traditional end-point method utilizing I_{end} alone. Large deviations occur at high concentrations beyond the hook effect. **B**. Measured vs known hCG concentrations using the newly developed time-lapse method utilizing I_{end} and '*b*'. The new method enables accurate measurement over the entire range of hCG concentrations. All error bars represent standard deviations (N=3).

Discussion

LFIAs are powerful tools for POC diagnostics because of their low cost and simple visual end point detection and have gained tremendous commercial and clinical success over the past few decades (21, 22). In recent years, smart phones have become ubiquitous and the power of smart phone imaging is widely being harnessed for point-of-care diagnostics (23–25). Smart phones have already been used to draw quantitative results from LFIAs (26–28). We envision that with the power of time-lapse imaging afforded by modern smart phones, additional functionality may be added to pre-existing commercial LFIAs. An important feature of LFIAs is their dynamic range for analyte quantification. Several LFIA design modifications have previously been proposed for expanding the dynamic range (11, 16–19). However, even a slight design modification causes a long-time delay in testing and manufacturing. In contrast, the method we propose in this article enables expansion of the dynamic range of off-the-shelf pre-existing LFIAs.

In theory, our proposed method can be used with any commercially available LFIA. However, some LFIAs presented challenges in real time imaging because they have not been optimized for that purpose. We utilized our method for quantifying hCG concentrations from two other commercial home pregnancy tests, ‘Prega’ and ‘i-Can’, and faced certain difficulties. In i-Can, the nitrocellulose strips were placed upside down such that the plastic-backed side of strips faced upward, which caused reflection of light and prevented acquiring appropriate images. This issue can be eliminated by inverting the nitrocellulose strip within the housing at the time of manufacturing (in most LFIAs, the plastic side faces downward). In Prega, the gold-nanoparticles stored in the conjugate pad moved as a concentrated (dark red) plug through the membrane. While the plug ultimately flowed into the wicking pad revealing test and control lines, critical real time information of test and control line development was lost during the

process. The plug formation could be a result of excessive gold nanoparticles loaded into the conjugate pad, most of which did not adhere to the test or control lines and flowed into the wicking pad. This issue could be alleviated by reducing the loading of gold nanoparticles in the conjugate pad.

Certain simplifying assumptions were made during modelling transport phenomena at the test and control lines. First, the flow velocity was assumed to be constant (v = 0.3333 mm s^{-1}) throughout. In reality, as the fluid front wicks through the nitrocellulose membrane, there is a continuous reduction in the velocity, which is explained by the well-established Washburn equation (29). However, once the fluid front reaches the wicking pad, the velocities are known to be pseudo steady (30). In experiments, the fluid fronts reached the wicking pads in ~25s, whereas signals continued to develop over 600s. Therefore, the reduction in velocity occurs only over a short fraction of the entire experiment and the assumption of constant velocity is reasonable. The other important assumption is that a well-mixed antigen gold nanoparticle conjugate solution enters the test strip. In experiments, the gold nanoparticles are stored in a conjugate pad and are released as a plug. Therefore, the modelling assumption reduces to the assumption that the antigen solution mixes well with the dried reagents in the conjugate pad and that the mixed solution is released continuously over the entire test period. While the latter assumption may be slightly flawed given the plug release in experiments, it is only faulty towards the end of the test. Because most of the relevant dynamic events that determine analyte concentration occur within the first 200s (Figure 3*C* and Supplementary Information Section S4), this assumption is reasonable. Several previous models of transport phenomena at the test line have made a similar assumption (16, 17). We would also like to add that the biexponential form in Eq. 2 is just one of the forms that can be used for fitting time profiles of T/C ratio and, in theory, other forms could be used. However, we tried several other forms, e.g. polynomial

(3^{rd}, 4^{th} and 5^{th} orders), one-term and two-term power series, and Gaussian, but only the biexponential form fit the entire range of *T/C* ratio vs time data.

Conclusion

This work presents theoretical understanding of how analyte concentration affects kinetic phenomena at test and control lines of a sandwich LFIA. This is the first report of modelling transport phenomena at the control line of an LFIA. The model revealed parameters, the evaluation of which enabled expanding the dynamic range of unmodified commercial LFIAs from 1.5 to 3 orders of magnitude using a time lapse app on a smartphone. Considering the ubiquity of smartphones, this method promises to further expand the utility of the LFIA, an already successful and widespread modality of point-of-care diagnostic testing.

References

1. S. Shin, M. Choi, J. Shim, S. Park, Hook effect detection and detection-range-controllable one-step immunosensor for inflammation monitoring. *Sensors Actuators B Chem.* **304**, 127408 (2020).
2. S. Yener, A. Comlekci, N. Arda, S. Men, S. Yesil, Misdiagnosis due to the Hook Effect in Prolactin Assay. *Med. Princ. Pract.* **17**, 429–431 (2008).
3. J. Oh, H. A. Joung, H. S. Han, J. K. Kim, M. G. Kim, A hook effect-free immunochromatographic assay (HEF-ICA) for measuring the C-reactive protein concentration in one drop of human serum. *Theranostics* **8**, 3189–3197 (2018).
4. R. Leboeuf, M.-F. Langlois, M. Martin, C. E. Ahnadi, G. D. Fink, “Hook Effect” in Calcitonin Immunoradiometric Assay in Patients with Metastatic Medullary Thyroid Carcinoma: Case Report and Review of the Literature. *J. Clin. Endocrinol. Metab.* **91**, 361–364 (2006).
5. L. Anfossi, *et al.*, Development and application of a quantitative lateral flow immunoassay for fumonisins in maize. *Anal. Chim. Acta* **682**, 104–109 (2010).
6. J. Soon, *et al.*, Development of a point-of-care assay system for high-sensitivity C-reactive protein in whole blood. **332**, 51–59 (2003).
7. D. J. Gasperino, *et al.*, Threshold-Based Quantification in a Multiline Lateral Flow Assay via Computationally Designed Capture Efficiency. *Anal. Chem.* **90**, 6643–6650 (2018).

8. L. Gervais, E. Delamarche, Toward one-step point-of-care immunodiagnostics using capillary-driven microfluidics and PDMS substrates †. **9** (2009).

9. L. Jaffe, KINETICS OF TWO-SITE THE IMMUNORADIOMETRIC ASSAY S-II. **15**.

10. M. J. Khosravi, Shifting the "hook effect" in one-step immunometric assays. *Clin. Chem.* (1990).

11. L. Zhan, *et al.*, The Role of Nanoparticle Design in Determining Analytical Performance of Lateral Flow Immunoassays (2017) https:/doi.org/10.1021/acs.nanolett.7b02302.

12. S. Amarasiri Fernando, G. S. Wilson, Studies of the "hook" effect in the one-step sandwich immunoassay. *J. Immunol. Methods* **151**, 47–66 (1992).

13. Y. K. Oh, H. A. Joung, H. S. Han, H. J. Suk, M. G. Kim, A three-line lateral flow assay strip for the measurement of C-reactive protein covering a broad physiological concentration range in human sera. *Biosens. Bioelectron.* **61**, 285–289 (2014).

14. H. A. Graham, P. Lisi, P. E. Marantz, United States Patent (19) (1988).

15. E. Rey, D. O. Dell, S. Mehta, D. Erickson, Mitigating the hook effect in lateral flow sandwich immunoassays using real- time reaction kinetics. *Anal. Chem.* **89**, 5095–5100 (2017).

16. S. Qian, H. H. Bau, A mathematical model of lateral flow bioreactions applied to sandwich assays. *Anal. Biochem.* **322**, 89–98 (2003).

17. M. S. Ragavendar, C. M. Anmol, A mathematical model to predict the optimal test line location and sample volume for lateral flow immunoassays. *2012 Annu. Int. Conf. IEEE Eng. Med. Biol. Soc.*, 2408–2411 (2012).

18. D. V Sotnikov, A. V Zherdev, B. B. Dzantiev, Mathematical Modeling of Bioassays. **82**, 1744–1766 (2017).

19. Z. Liu, *et al.*, Sensors and Actuators B : Chemical The effect of report particle properties on lateral flow assays : A mathematical model. *Sensors Actuators B. Chem.* **248**, 699–707 (2017).

20. C. H. Lin, *et al.*, Quantitative measurement of binding kinetics in sandwich assay using a fluorescence detection fiber-optic biosensor. *Anal. Biochem.* **385**, 224–228 (2009).

21. T. R. Kozel, A. R. Burnham-Marusich, Point-of-Care Testing for Infectious Diseases: Past, Present, and Future. *J. Clin. Microbiol.* **55**, 2313 LP – 2320 (2017).

22. H. Kim, D.-R. Chung, M. Kang, A new point-of-care test for the diagnosis of infectious diseases based on multiplex lateral flow immunoassays. *Analyst* **144**, 2460–2466 (2019).

23. T. Alawsi, Z. Al-Bawi, A review of smartphone point-of-care adapter design. *Eng. Reports* **1**, e12039 (2019).

24. C. Liang, *et al.*, Smartphone-app based point-of-care testing for myocardial infarction

biomarker cTnI using an autonomous capillary microfluidic chip with self-aligned on-chip focusing (SOF) lenses. *Lab Chip* **19**, 1797–1807 (2019).

25. X. Xu, *et al.*, Advances in Smartphone-Based Point-of-Care Diagnostics. *Proc. IEEE* **103**, 236–247 (2015).

26. C. Ruppert, N. Phogat, S. Laufer, M. Kohl, H.-P. Deigner, A smartphone readout system for gold nanoparticle-based lateral flow assays: application to monitoring of digoxigenin. *Microchim. Acta* **186**, 119 (2019).

27. Z. Rong, *et al.*, Smartphone-based fluorescent lateral flow immunoassay platform for highly sensitive point-of-care detection of Zika virus nonstructural protein 1. *Anal. Chim. Acta* **1055**, 140–147 (2019).

28. K. H. Foysal, S. E. Seo, M. J. Kim, O. S. Kwon, J. W. Chong, Analyte Quantity Detection from Lateral Flow Assay Using a Smartphone. *Sensors* **19** (2019).

29. E. W. Washburn, The Dynamics of Capillary Flow. *Phys. Rev.* **17**, 273–283 (1921).

30. S. Mendez, *et al.*, Imbibition in porous membranes of complex shape: quasi-stationary flow in thin rectangular segments. *Langmuir* **26**, 1380–1385 (2010).

Acknowledgements

This work was supported by the Science and Engineering Research Board (SERB, India) in the form of an Extramural Research Grant (EMR/2016/006029) and the Department of Biotechnology (DBT, India) in the form of an Innovative Young Biotechnologist Award (BT/010/IYBA/2016/07) to BJT.

Author Contributions

B.J.T conceived and designed the work and contributed towards analysis and interpretation of data. N.S conducted all experiments, mathematical modelling, and contributed towards analysis and interpretation of data, and prepared all figures. B.J.T and N.S together wrote the main manuscript text.

SUPPLEMENTARY INFORMATION (SI)

S1. Image acquisition and analysis

Rectangular regions of interest (ROIs) were created around the test and control lines and ROIs of equal size were created immediately upstream and immediately downstream of the test and control lines for measurement and subtraction of background signals. At each time point, test and control line intensities were calculated by averaging intensities over the test and control zones and subtracting intensities from the corresponding backgrounds as shown in Fig. S1.

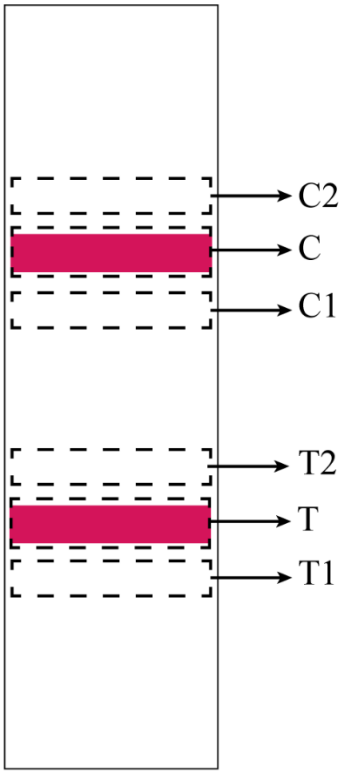

Intensity	Test	Control
Measured	T	C
Background	TB = (T1+T2)/2	CB = (C1+C2)/2
Actual	T-TB	C-CB

Figure S1: Schematic representation of image analysis technique

S2. Modelling of lateral flow immunoassay

The transport-reaction equation of each species can be written as follows (1)

$$\frac{\partial C_A}{\partial t} = D_A \frac{\partial C_A^2}{\partial x^2} - v.\left(\frac{\partial C_A}{\partial x}\right) - F_{RA} - F_{PA} - F_{QPA}^2 \quad \text{---- Eq. S1}$$

$$\frac{\partial C_P}{\partial t} = D_P \frac{\partial C_P^2}{\partial x^2} - v.\left(\frac{\partial C_P}{\partial x}\right) + F_{RPA}^2 - F_{PA} - F_{QP} \quad \text{---- Eq. S2}$$

$$\frac{\partial C_{PA}}{\partial t} = D_{PA} \frac{\partial C_{PA}^2}{\partial x^2} - v.\left(\frac{\partial C_{PA}}{\partial x}\right) - F_{RPA}^1 + F_{PA} - F_{QPA}^1 \quad \text{---- Eq. S3}$$

$$\frac{\partial C_{RA}}{\partial t} = F_{RA} \quad \text{---- Eq. S4}$$

$$\frac{\partial C_{RPA}}{\partial t} = F_{RPA} \quad \text{---- Eq. S5}$$

$$\frac{\partial C_{QP}}{\partial t} = F_{QP} \quad \text{---- Eq. S6}$$

$$\frac{\partial C_{QPA}}{\partial t} = F_{QPA} \quad \text{---- Eq. S7}$$

where '$D_A = 10^{-10} m^2 s^{-1}$' and '$D_{PA} = 10^{-12} m^2 s^{-1}$' were the diffusion co-efficient of analyte (A) and analyte-detection antibody complex (PA) respectively (1). The initial capture antibody concentration was assumed to be 10^{-8} M to approximately match the experimentally spotted concentration at test (R_0) and control lines (Q_0). The analyte concentration, C_A was varied from 10^{-10} *to* 10^{-5} M. The reaction rate of various species are as follows,

$$F_{PA} = k_{a1} C_A C_P - k_{d1} C_{PA} \quad \text{---- Eq. S8}$$

$$F_{RA} = k_{a2} C_A (R_o - C_{RA} - C_{RPA}) - k_{d2} C_{RA} - k_{a4} C_{RA} C_P + k_{d4} C_{RPA} \quad \text{---- Eq. S9}$$

$$F_{RPA}^1 = k_{a3} C_{PA} (R_o - C_{RA} - C_{RPA}) - k_{d3} C_{RPA} \quad \text{---- Eq. S10}$$

$$F_{RPA}^2 = k_{a4} C_{RA} C_P - k_{d4} C_{RPA} \quad \text{---- Eq. S11}$$

$$F_{RPA} = F_{RPA}^1 + F_{RPA}^2 \quad \text{---- Eq. S12}$$

$$F_{QP} = k_{a5} C_P \left(Q_o - C_{QP} - C_{QPA}\right) - k_{d5} C_{QP} - k_{a5} C_{QP} C_A + k_{d5} C_{QPA} \quad \text{---- Eq. S13}$$

$$F_{QPA}^1 = k_{a6} C_{PA} \left(Q_o - C_{QP} - C_{QPA}\right) - k_{d6} C_{QPA} \quad \text{---- Eq. S14}$$

$$F_{QPA}^2 = k_{a7} C_{QP} C_A - k_{d7} C_{QPA} \quad \text{---- Eq. S15}$$

$$F_{QPA} = F_{QPA}^1 + F_{QPA}^2 \quad \text{---- Eq. S16}$$

where the $k_{ai(i=1\ to\ 7)}\ and\ k_{bi(i=1\ to\ 7)}$ were the forward and backward reaction rate constants respectively. The values of forward and backward rate constants for analyte-antibody interactions for the test line were obtained from Qian et al (1), $k_{a1} = k_{a2} = k_{a3} = k_{a4} = 10^6\ M^{-1}s^{-1}$ and $k_{b1} = k_{b2} = k_{b3} = k_{b4} = 10^{-3}\ M^{-1}s^{-1}$, respectively, whereas the values of forward and backward rate constants for mouse IgG anti-mouse IgG interactions for the control line were $k_{a5} = k_{a6} = k_{a7} = 10^5\ M^{-1}s^{-1}$ and $k_{b5} = k_{b6} = k_{b7} = 10^{-4}\ M^{-1}s^{-1}$ respectively (2).

The inlet (at x = 0 cm) conditions were

$$C_A = C_{A0};\ C_P = C_{P0}; C_{PA} = 0; \qquad \text{---- Eq. S17}$$

At the outlet (at x = 2 cm) conditions were

$$\frac{\partial C_A}{\partial x} = \frac{\partial C_P}{\partial x} = \frac{\partial C_{PA}}{\partial x} = 0 \qquad \text{---- Eq. S18}$$

And the initial conditions were

$$C_A = C_P = C_{PA} = C_{RA} = C_{RPA} = C_{QPA} = C_{QP} = 0 \qquad \text{---- Eq. S19}$$

$$C_{RA} = \begin{cases} r_o & (x_{l1} < x < x_{l2}), \\ 0 & elsewhere \end{cases} \qquad \text{---- Eq. S20}$$

$$C_{QA} = \begin{cases} q_o & (x_{l3} < x < x_{l4}), \\ 0 & elsewhere \end{cases} \qquad \text{---- Eq. S21}$$

S3. Finite Central Difference Method for Spatial Discretization

The transport-reaction equations (S1 - S7) and the initial and boundary conditions (S17 - S21) were discretized by using the central difference scheme. Uniform grid space (Δx = 0.01) was

used along the length of the modelling domain except at test and control line region where a very fine grid space ($\Delta x = 0.0005$) was used.

S4. Experimental profiles of T/C ratio

The experimental *T/C* ratio for different hCG concentrations had different time profiles for low, high and very high analyte concentrations (Fig. S2). For low analyte concentrations (2.5 to 10 IU/mL), the *T/C* ratio increased monotonously; for high analyte concentrations (30 to 100 IU/mL), the *T/C* ratio initially increased and then decreased; for very high analyte concentrations (200 to 500), the T/C ratio decreased monotonously (Fig. S2).

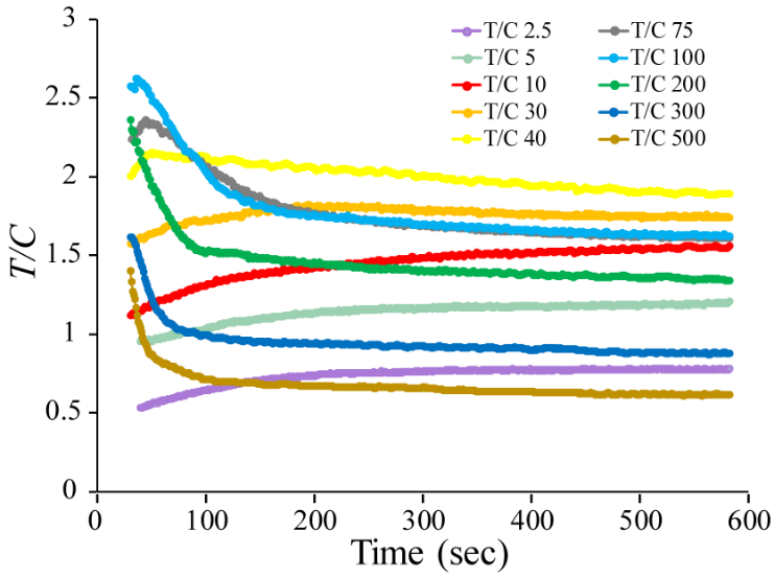

Figure S4: Experimental profiles of T/C ratio for different hCG concentration.

References

1. S. Qian, H. H. Bau, A mathematical model of lateral flow bioreactions applied to sandwich assays. **322**, 89–98 (2003).

2. C. H. Lin, *et al.*, Quantitative measurement of binding kinetics in sandwich assay using a

fluorescence detection fiber-optic biosensor. *Anal. Biochem.* **385**, 224–228 (2009).